High performance semiconducting nanosheets *via* a scalable powder-based electrochemical exfoliation technique

Rebekah A. Wells[1], Miao Zhang[2], Tzu-Heng Chen[2], Victor Boureau[3], Marina Caretti[1], Yongpeng Liu[1], Jun-Ho Yum[1], Hannah Johnson[1,4], Sachin Kinge[4], Aleksandra Radenovic[2], Kevin Sivula[1]*

[1] *Laboratory for Molecular Engineering of Optoelectronic Nanomaterials (LIMNO), Institute of Chemical Sciences and Engineering, École Polytechnique Fédérale de Lausanne, 1015 Lausanne, Switzerland*

[2] *Laboratory of Nanoscale Biology (LBEN), Institute of Bioengineering, École Polytechnique Fédérale de Lausanne (EPFL), 1015, Lausanne, Switzerland*

[3] *Interdisciplinary Center for Electron Microscopy (CIME), EPFL, Lausanne 1015, Switzerland*

[4] *Advanced Materials Research, Toyota Motor Europe, B-1930 Zaventem, Belgium*

ABSTRACT. The liquid-phase exfoliation of semiconducting transition metal dichalcogenide (TMD) powders into 2D nanosheets represents a promising route towards the scalable production of ultrathin high-performance optoelectronic devices. However, the harsh conditions required negatively affect semiconducting properties leading to poor device performance. Herein we demonstrate a gentle exfoliation method employing standard bulk MoS_2 powder (pressed into pellets) together with the electrochemical intercalation of a quaternary alkyl ammonium. Resulting nanosheets are produced in high yield (32%) and consist primarily of mono-, bi-, tri-atomic layers with large lateral dimensions (>1 µm), while retaining the semiconducting polymorph. Exceptional optoelectronic performance of nanosheet thin-films is observed such as enhanced photoluminescence, charge carrier mobility (up to 0.2 cm^2 V^{-1} s^{-1} in a multi-sheet device), and photon-to-current efficiency while maintaining high transparency (>80%). Specifically, as a photoanode for iodide oxidation, an internal quantum efficiency up to 90% (at +0.3 V vs Pt) is achieved (compared to only 12% for MoS_2 nanosheets produced *via* ultrasonication). Further using a combination of fluorescence microscopy and high-resolution scanning transmission electron microscopy (STEM) we show that our gently exfoliated nanosheets possess a defect density (2.33 $\times$ 10^{13} cm^{-2}) comparable to monolayer MoS_2 prepared by vacuum-based techniques and at least four times less than ultrasonicated MoS_2 nanoflakes. Finally, we expand this method towards other TMDs (WS_2, WSe_2) to demonstrate its versatility towards high-performance and fully scalable van der Waals heterojunction devices.

2

TOC IMAGE
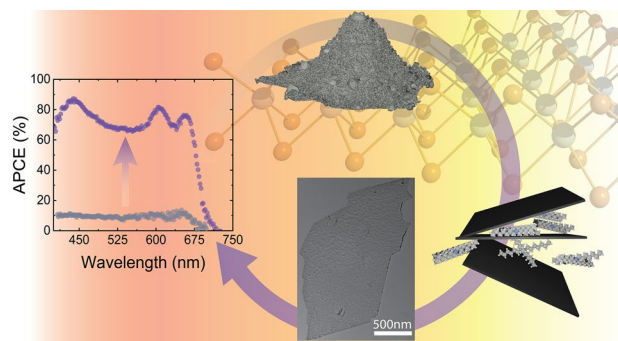
INTRODUCTION

Ultrathin "two-dimensional" (2D) nanosheets of semiconducting transition metal dichalcogenides (2D TMDs) with the chemical formula MX_2 (X = S, Se, *etc. M* = W, Mo, *etc.*) are promising materials for next-generation optoelectronic devices including transistors, light emitting diodes, and sensors, thanks to their exceptional semiconducting properties and intrinsic stability.[1–4] These attractive properties together with the earth abundance of their atomic components also makes them particularly attractive for large-scale applications requiring robust semiconductors such as photovoltaic, photoelectrochemical, or photocatalytic energy conversion at a globally-relevant scale.[5–8] Towards this goal, significant research efforts have been directed towards the fabrication of large-area, low-cost 2D TMD films.[9–12]

When considering the scalability and cost-effectiveness of 2D TMD film fabrication, liquid-phase exfoliation techniques that employ bulk powders of micrometer-sized TMD particles[13] have a clear advantage over techniques that employ high-vacuum processes (such as chemical vapor deposition (CVD) [14,15] and molecular beam epitaxy (MBE)[16]), or exfoliation methods that require large single crystals as starting material (*e.g.* mechanical exfoliation[17]). Indeed micron-sized crystalline powders of TMDs can be readily synthesized at large scales[18] and can be easily exfoliated into optoelectronically active 2D nanoflakes or nanosheets dispersed in solution using

3

ultrasonication,[13,19–21] shear,[22] or chemical exfoliation (*via* Li ion intercalation).[23,24] The resulting 2D nanomaterial dispersions can then be easily processed into thin films using scalable roll-to-roll techniques.[9]

However, despite the versatility of the current liquid phase exfoliation approaches, the semiconducting performance of the produced nanosheets are drastically decreased by the harsh nature of these exfoliation methods.[23,25–28] Indeed, ultrasonication or shear methods break *MX* bonds within the 2D layers leading to nanoflakes with small lateral dimensions as well as a high concentration of chalcogenide vacancies,[20,26,28] and chemical exfoliation techniques lead to a conversion of the semiconducting 2H crystal phase of the TMD sheets to the semimetallic 1T form, thus destroying the semiconducting properties.[23,29–31] While significant efforts have been directed to healing defects and repairing the semiconducting properties of liquid-phase exfoliated 2D TMDs,[23,27,31–36] most reported procedures require aggressive chemical, heating, or laser treatments in the solid state, which limits the versatility and scalability of the overall process. Moreover, the performance of defect-treated 2D nanoflakes generally remains poor[23] compared to nanosheet preparation methods that maintain the pristine 2H-phase throughout processing, or that produce it directly (*e.g.* CVD or MBE). Thus, despite significant efforts developing approaches for the liquid phase exfoliation of bulk TMD powders, there remains a clear need to realize a procedure that can yield high quality semiconducting TMD nanosheets directly *via* a scalable exfoliation procedure.

Electrochemically-driven intercalation techniques have the potential to offer scalable production of TMD nanosheets,[31,37–39] and moreover recent reports using bulk single crystals[11,40] of TMDs have suggested that high-quality semiconducting 2D nanosheets can be produced with an electrochemical intercalation technique employing bulky organic cations. While promising, these processes are fundamentally limited by the difficulty of producing large-sized bulk single crystal

4

TMDs. Herein we leverage the electrochemical intercalation approach using a bulky organic cation and present a versatile method for the gentle exfoliation of TMDs starting with commercially-available TMD powders. We show that MoS_2 nanosheet thin films produced from our method exhibit exceptional optoelectronic performance and we further demonstrate that our technique is suitable for exfoliating a range of TMD materials including MoS_2, WSe_2, and WS_2.

RESULTS AND DISCUSSION

Electrochemical intercalation/exfoliation of pressed powder pellets

To demonstrate our powder-based intercalation-exfoliation technique we use MoS_2 as a model TMD material due to its well-documented challenges with the 1T-phase transition as well as its promising application for solar-energy conversion devices.[41,42] Figure 1 illustrates the full process of our electrochemical pellet intercalation (ECPI) exfoliation method. First, commercially available micrometer-sized powder is pressed into a pellet using a standard hydraulic press. The pellet is then annealed (1100°C for 48 hours) under the presence of excess sulfur (3:1 molar ratio MoS_2:S) to increase the mechanical robustness and electrical conductivity of the pellet. Indeed, larger crystalline domains are observed by scanning electron microscopy of the annealed pellet compared to the unannealed case (see Figure S1, supporting information (SI)), and qualitative investigation of the pellet electronic conductivity shows little resistance across the annealed pellet compared to unannealed pellet. The annealed pellet is then connected to a potentiostat as the working electrode using a metal clip and submerged into an acetonitrile-based electrolyte containing tetraheptylammonium (THA^+) bromide, so chosen for its large size (20Å) compared to the interlayer spacing of MoS_2 (6.1 Å), and to avoid phase-changes as a result of electron injection [11] A glassy carbon rod is used as the counter electrode and a bias of 10 V is applied causing THA^+

5

intercalation in the MoS$_2$ pellet cathode and bromide oxidization to bromine on the anode. As

intercalation proceeds, the electrolyte turns yellow due to bromine formation while areas of the

pellet in contact with the solution can be seen to visibly expand (Figure S2 and S3, SI).

Intercalation of MoS$_2$ with THA$^+$ is confirmed with cyclic voltammetry (CV), X-ray diffraction

spectroscopy (XRD), and energy dispersive X-ray spectroscopy (EDS) (see Figure S4, SI).

Periodically, these intercalated, expanded parts detach from the pellet exposing unintercalated

areas of the pellet for subsequent intercalation (see Video S1, SI). In principle, this sloughing

feature is an advantage over methods employing bulk single crystals where the single crystal

cathode remains intact throughout the intercalation process. Additionally, since the detached

material is both intercalated and partially exfoliated, complete exfoliation into nanosheets requires

only gentle agitation (bath sonication in N-Methylpyrrolidone (NMP)), compared to the high-

powered tip-probe sonication as described in single crystal demonstrations.[11,40]
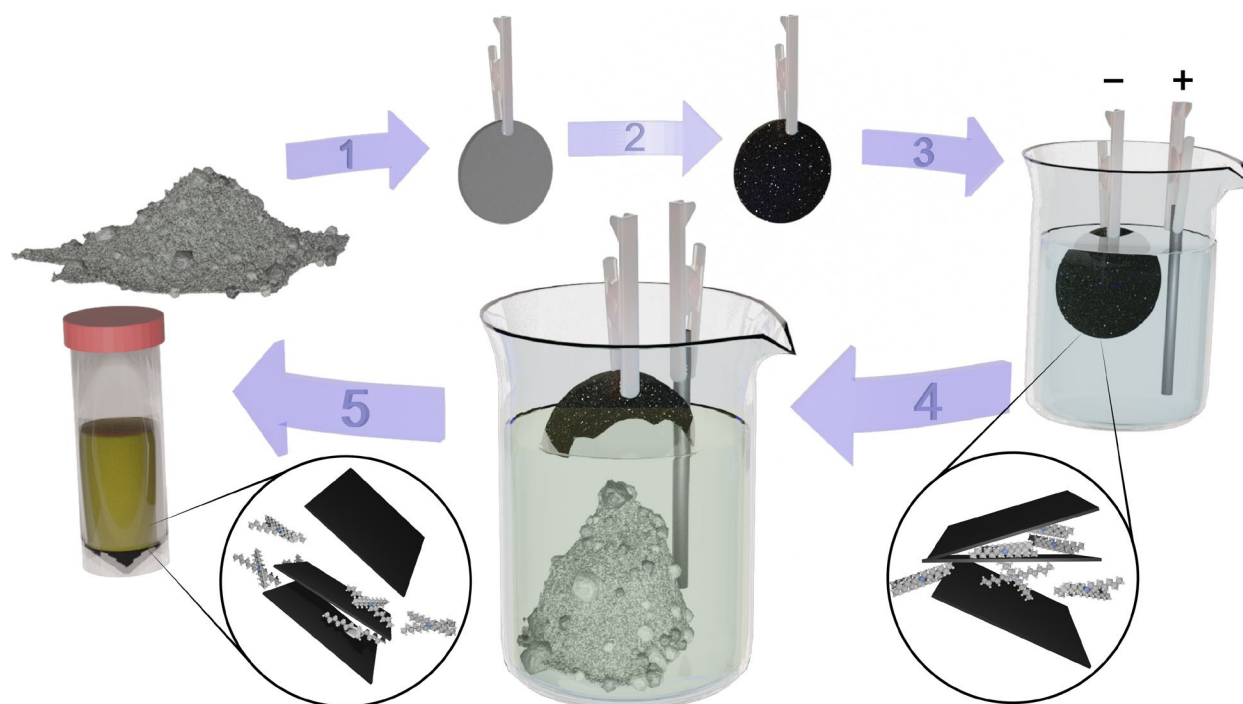
Figure 1. Schematic of the electrochemical pellet intercalation (ECPI) exfoliation method. (1) As-received MoS_2 powder is pressed into a pellet. (2) The pellet is annealed at 1100 °C for 48 hours with excess S vapor. (3) The pellet is immersed in a solution of tetraheptylammonium bromide (THA^+B^-) with a glassy carbon rod counter electrode. (4) Operating the pellet as a cathode causes THA^+ intercalation and the sloughing of intercalated MoS_2. (5) The intercalated powder is collected, rinsed, agitated, and finally centrifuged at low speed to remove remaining bulk material. The result is a viscous, green-brown solution of exfoliated MoS_2 nanosheets.

Notably the presence of N-Methylsuccinimide (NMS), a side product of the high-power ultrasonication of NMP,[25] is absent in our bath agitation approach (Figure S5, SI) confirming the gentler nature of the process and eliminating the problem of NMS contamination. After exfoliation, low-speed centrifugation is carried out to remove any unexfoliated bulk powder, leaving a viscous greenish-brown solution (see Figure S6, SI). We note that no further nanosheet size selection is performed to isolate monolayers, or remove the smallest, optoelectronically inactive nanoparticles, like is typically performed with ultrasonication approaches.[27] Though the ECPI exfoliation method can be easily adjusted (see Methods section), we typically start with 500 mg of as-received MoS_2 powder and end with 8 mL of a dispersion with a concentration of around 20 mg mL^{-1} corresponding to a single pass yield of 32%. While yield is subject to numerous adjustable processing parameters, namely centrifugation time and speed, our yield is similar to reports for high-power ultrasonication and higher than studies on shear or hybrid chemical intercalation-ultrasonication methods (See Table S1).[22,24,26,28]

Nanosheet characterization

To verify the success of our ECPI exfoliation method, we next extensively characterized the resulting MoS_2 nanosheets. Transmission electron microscopy (TEM) was first used to examine drop-casted nanosheet dispersions. This revealed the presence of pristine, thin MoS_2 nanosheets with lateral dimensions greater than 1 μm, as seen in Figure 2a, that have selected area electron diffraction (SAED) patterns confirming the semiconducting $2H-MoS_2$ structure (see Figure 2b). In order to understand the relative abundance of such large, thin sheets (compared to smaller fragments) the MoS_2 dispersion was processed into a thin film using a liquid-liquid interfacial self-assembly (LLISA) technique as described previously,[8,9] which produces a single layer of MoS_2 nanosheets on a desired substrate and allows hundreds of individual flakes to be characterized simultaneously. The number of atomic layers in each nanosheet was investigated using high-angle annular dark field (HAADF) scanning TEM (STEM), a technique sensitive to the thickness of thin samples,[43] and the presence of monolayer nanosheets was further verified by atomic force microscopy (See Figure S7, SI). The HAADF STEM image in Figure 2c was color-coded with respect to the number of atomic layers. Images showing isolated mono-, bi-, and trilayers, were extracted from the HAADF-STEM image (Figure 2c) and are displayed in Figure 2d, 2e, and 2f, respectively. These images facilitated the estimation of the nanosheet area distributions for each nanosheet layer population. Statistical results of the size estimation of over 150 nanosheets are displayed in the form of a histogram in Figure 2g. Notably, unlike previous observations with nanoflakes exfoliated by ultrasonication[8,27,28,32,36], the ECPI exfoliation method produces a majority of monolayer sheets over the entire nanosheet area range observed.
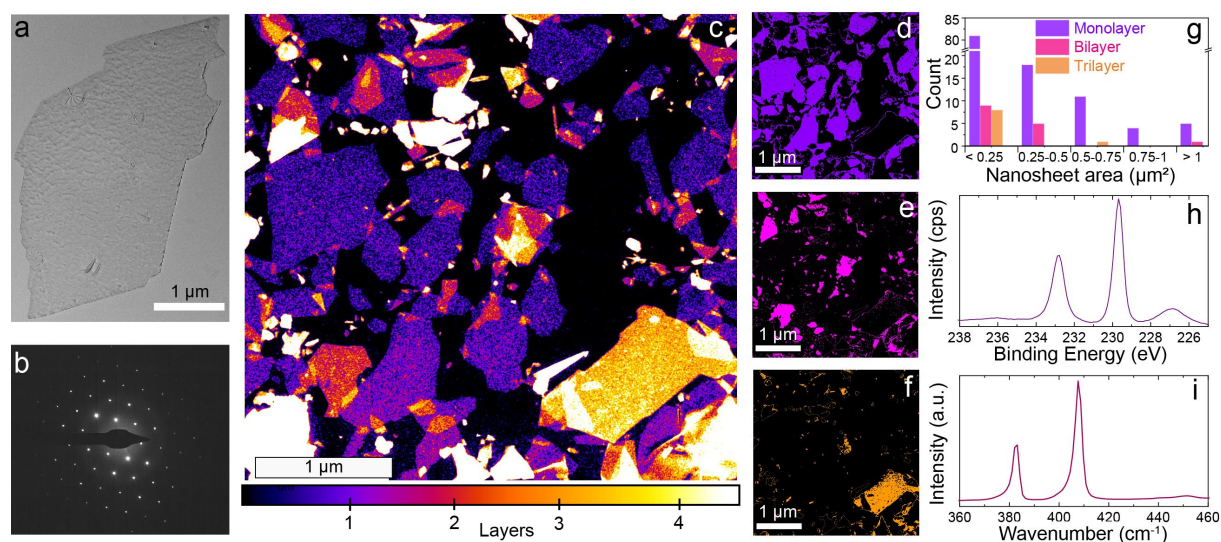
Figure 2. (a) TEM image and (b) selected area electron diffraction pattern of an ECPI-made MoS_2 nanosheet. (c) HAADF STEM image of a thin film of ECPI-made MoS_2 nanosheets. The color-scale highlights thickness differences in the flakes: purple for monolayer, pink for bilayer or overlapping monolayers, yellow for trilayers of overlapping mono/bi-layers, and white (saturated contrast) for regions greater than three layers. For better visualization the flakes have been separated according to thicknesses and are shown with the same color scale in (d), (e), and (f). (g) Histogram of the nanosheet populations as a function of nanosheet area. The pristine nature of the nanosheets is confirmed by (h) XPS and (i) Raman spectroscopy (see main text for references).

More specifically, we note that previous descriptions of the liquid phase exfoliation of TMDs have consistently reported a similar relationship between nanoflake lateral size and number of atomic layers (nanoflake thickness) where monolayers have smallest dimensions and larger dimensions are only possible with thicker flakes.[26–28,44] This has been explicitly discussed for

nanoflakes produced by ultrasonication exfoliation,[26] and it is likely linked to the anisotropic mechanical properties of the layered TMDs (stemming from the layered crystal structure). In stark contrast, our ECPI exfoliation method is capable of producing very thin flakes (mono-, bi-, trilayers) with large lateral dimensions ($> 1 \ \mu m^2$) while nanosheets with more than three atomic layers mostly occupy the smallest area range ($< 0.25 \ \mu m^2$, see Figure S7, SI). It is reasonable to conclude that, since the ECPI exfoliation method does not rely on mechanical forces to exfoliate the TMD layers[11], the resulting nanosheet size distribution does not have the same limitations as other powder-based exfoliation methods (See Table S1).

To further verify the quality of the ECPI exfoliated MoS_2 nanosheets, molybdenum core level X-ray photoelectron spectroscopy (XPS) and Raman spectroscopy of the LLISA-deposited nanosheet films were performed, and the results are shown in Figure 2h and 2i, respectively. The XPS spectrum displays peaks from the Mo3d level at 229.7 eV and 232.7 eV and one peak from the S2s orbital at 227.2 eV, which are in good agreement with the accepted references for pristine material.[45] Moreover, the deconvolution and fitting of the spectrum showed no trace of 1T-phase MoS_2 (see Figure S6a, SI), and no contribution from Br is recorded, suggesting that there is no detectable contamination from the THA^+ bromide (Figure S8). Lastly, the Raman spectrum (which is an average over many nanosheets, see Methods section) displays two peaks corresponding to the in-plane E^1_{2g} and out-of-plane A_{1g} modes at 384 cm^{-1} and 409 cm^{-1}, respectively. No peaks corresponding to the 1T-phase (154 cm^{-1}, 219 cm^{-1}, or 327 cm^{-1})[46] were observed. These values confirm the pristine nature of the film despite the mix of the nanosheet dimensions.

Defect mapping of ECPI and ultrasonicated nanosheets

It is well understood that preserving the 2H semiconducting phase in MoS_2 is crucial for optoelectronic applications. Compared to chemical intercalation, which induces the semimetal 1T phase, our ECPI method is clearly superior as a scalable method for producing semiconducting nanomaterials. However, it is less clear if our gentle exfoliation technique holds a clear advantage over other 2H-preserving exfoliation methods, namely ultrasonication. To ascertain this, we prepared dispersions of ultrasonicated MoS_2 nanoflakes using a procedure previously optimized for producing material with high photoelectrochemical activity[9] and compared them to the ECPI-made nanosheets *via* a set of imaging techniques performed on thin films of nanoparticles deposited by the LLISA technique. Resulting images are shown in Figure 3.

HAADF STEM images for ECPI-produced nanosheet films and sonicated nanoflake films are shown in Figures 3a and 3c, respectively. Both the ECPI and ultrasonicated nanoparticle thin films show the nearly close-packed morphology that is typical of the LLISA deposition technique.[8,9,27,32] However, the ECPI-made nanosheet film appears nearly transparent against the background compared to the ultrasonicated nanoflakes, which appear generally brighter. This is because the ECPI-made nanosheets are very thin, interacting minimally with the electron beam while the ultrasonicated nanoflakes are thicker and therefore diffract the beam more strongly. Thus, despite each film being made up of a single layer of nanosheets or nanoflakes, the ultrasonicated nanoflakes contain more atomic layers than the ECPI-made nanosheets. This is further supported by analysis of UV-Vis spectra of the nanoflake dispersions used to make the films (Figure S9, SI) where a shift in the exiton peak location confirms a difference in average atomic layer numbers of the exfoliated nanoflakes/sheets. In addition to thickness differences, the ultrasonicated flakes have smaller lateral dimensions which is expected according to the previous reports discussed above. Indeed, a statistical distribution of the nanoflake size (Figure S9, SI) shows that the vast majority

11

(96%) of the ultrasonicated flakes are below 0.25 μm^2 in area. At higher magnifications (Figure

3b and 3d for ECPI and ultrasonicated nanomaterials, respectively) a clear difference is also noted

with respect to the presence of step-edge defects. While the ECPI-made nanosheets appear flat

with minimal edge steps, the ultrasonicated nanoflakes seem to consist of stacked atomic layers

with different lateral dimensions creating a large number of step-edges. Importantly, the presence

of step-edge defects is well-known to have a detrimental effect on the semiconducting properties

of TMDs.[47]
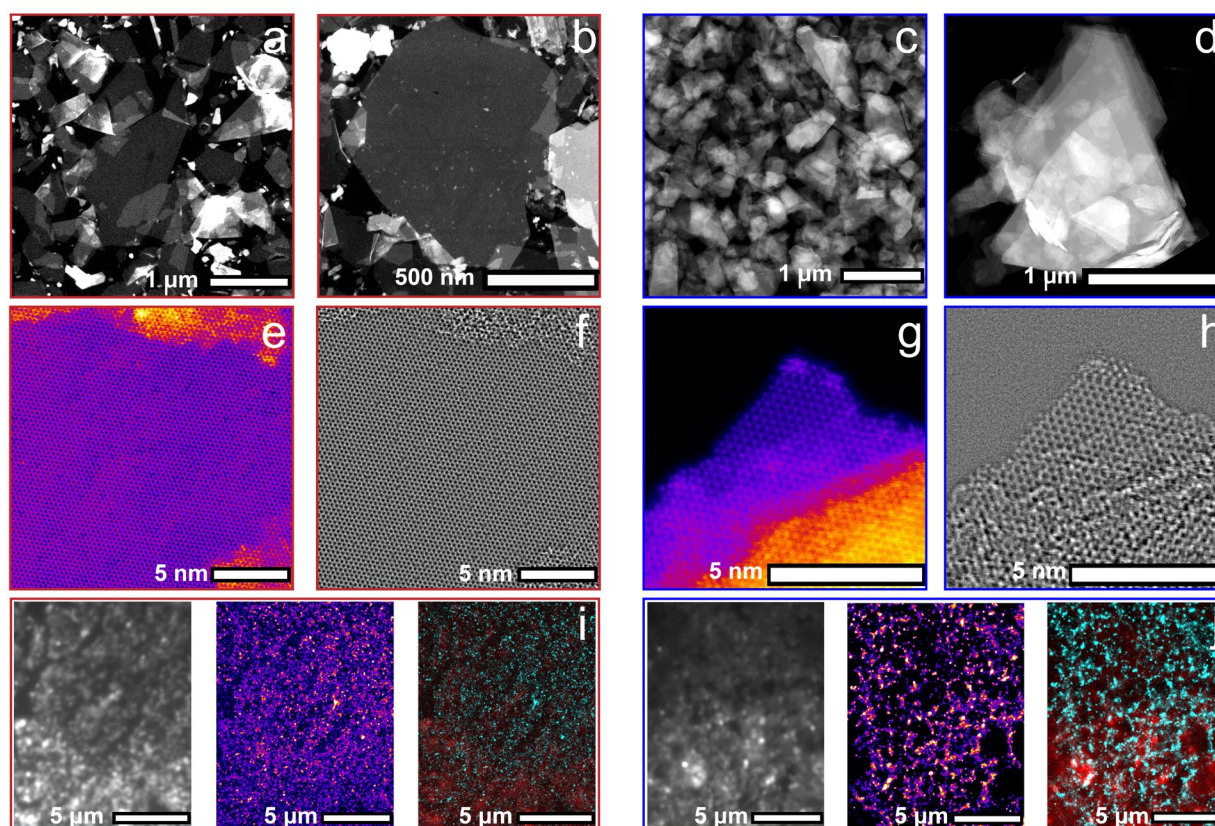
Figure 3. HAADF STEM images for ECPI-made nanosheets (a, b) and sonicated (c, d) nanoflakes.

High Resolution (HR) STEM images for ECPI-made nanosheets (e, f) and sonicated (g, h)

nanoflakes. Brighter regions suggest thicker material that interacts more strongly with the electron

beam causing more diffraction. (e, g) are HAADF detector images which have been falsely colored

to highlight thickness differences. (f, h) are integrated differential phase contrast detector (iDPC) images which allow clearer visualization of crystal defects and adatom contamination. Results of 2D-PAINT method for mapping defects on films of (i) ECPI-made nanosheets and (j) sonicated nanoflakes. Grayscale images show the PL for the 2D MoS_2 (left), heatmap images show the number of the detected probe-defect binding events (center), and cyan-red maps show the probe-defect binding events (cyan) overlayed on the 2D MoS_2 PL (red) to show probe location with respect to MoS_2 (right).

Differences in the defect concentration of the nanomaterials produced by the two methods are further highlighted by high-resolution STEM imaging. Annular dark-field (ADF) images shown in Figures 3e and 3g (color highlights the thickness differences) were acquired simultaneously with integrated differential phase contrast (iDPC)[48] images shown Figures 3f and 3h for the ECPI-made and ultrasonicated MoS_2, respectively (additional images can be found in Figure S10, SI, for a more thorough comparison). Notably the iDPC technique is very sensitive to changes in height and contamination including adatoms.[48] From these images we conclude ECPI-made nanosheets do indeed possess flat basal planes as well as clean lattices. As with CVD or PVD grown and mechanically exfoliated nanoflakes,[49–53] sulfur monovacancy point defects can be observed; however, it is important to note that it is challenging to differentiate intrinsic defects from those induced during imaging.[50,51] However, visual inspection of several flakes gives an average defect density of $2.3 \pm 0.6 \times 10^{13}$ cm^{-2}, which is comparable to—and in some cases less than—defect densities reported for CVD or PVD grown and mechanically exfoliated flakes.[51,53,54] In contrast,

given the irregular topography of the ultrasonicated nanoflakes, it is nearly impossible to find any large area of flat basal plane of a few atomic layers thickness for high-resolution STEM imaging (Figures 3g and 3h, Figure S8, SI). Moreover, the iDPC technique highlights high amounts of adatom contamination which appears worse (blurrier) at the step-edges. These two factors make identifying point defects challenging and quantifying them unfeasible on the ultrasonicated nanoflakes.

Given the difficulty to quantify the defect density difference between the MoS_2 nanomaterials produced with the two different exfoliation methods using electron microscopy imaging alone, we next employed a recently-reported non-destructive technique for the large-area mapping of defects in 2D TMDs using fluorescent molecular probes.[50] This method, called 2D-PAINT, is a variation of Points Accumulation for Imaging in Nanoscale Topography (PAINT) and relies on the specific interaction between a thiol functionality on the molecular probe and defects (sulfur vacancies and edge defects) in the nanosheets. Also on the probe, opposite of the thiol group, is a dye whose intermittent fluorescence is detected and imaged in an optical microscope. Applying the 2D-PAINT protocol to the solution-processed 2D MoS_2 nanosheets herein affords the relative quantification of the defect densities on an ensemble of nanoparticles. The results are shown for thin films of ECPI-produced (Figure 3i) and ultrasonicated nanoflakes (Figure 3j). The first panel (grayscale image) shows the normalized photoluminescence (PL) of the MoS_2 nanosheets themselves (not the molecular probe PL) observed in the 675-725 nm wavelength range (unnormalized images are shown in Figure S11). The second panel (colored heatmap) displays the number of detected probes (509-530 nm wavelength range) that have bound to defect sites on the MoS_2 nanosheets over the acquisition of 1000 frames. As observed in the heatmaps, a higher concentration of probe-defect binding events is observed for the sonicated nanoflake films. An

overlap of the PL of the MoS_2 flakes and the heatmap of the probe-defect binding events is shown in the third panel to better visualize the location of the probes with respect to the nanoflakes. To quantify the observed differences in probe-defect binding events, the event density rates were extracted for multiple areas of each film leading to an average probe-defect binding event density of 0.814 μm^{-1} frame^{-1} for the ultrasonicated flakes and 0.283 μm^{-1} frame^{-1} for ECPI-made sheets. Such an event density rate is proportional to the total defect density on the nanosheets. Thus, by using the 2D-PAINT method we find that ultrasonicated nanoflakes have roughly three times more defects compared to the ECPI-made nanosheets. However, due to the poorer dispersibility of the ultrasonicated nanoflakes, more aggregation was observed in the thin film, which likely leads to an underestimation of the defect density. In fact, spatial autocorrelation of the probe-defect binding event heatmaps, allows us to quantitatively describe the distribution of the probes *via* Moran's Index.[55] For a Moran's I value = 0 the events are considered a random spatial distribution while increasing values are associated with grouping or clumping.[55] A Moran's I value of 0.22 was recorded for the ECPI-made nanosheets and 0.44 for the ultrasonicated nanoflakes,[56] which is consistent with a more even distribution for the ECPI-made samples and more concentrated probe binding events for the sonicated samples. We note that the clumping experienced by the ultrasonicated flakes can potentially lead to over-crowded probe binding events that cannot be distinguished by 2D-PAINT, resulting in an underestimation of defects.

Nanosheet optoelectronic and photoelectrochemical performance

Having distinguished the ECPI-exfoliated nanosheets from the traditionally-produced ultrasonicated nanoflakes in terms of morphology and defects, we next sought to establish how these differences affect the optoelectronic performance of the semiconducting nanomaterial. Firstly, the UV-Visible and PL spectra of the ECPI-prepared and ultrasonicated nanosheet thin

films are displayed in Figure 4a. In terms of light absorption, despite both films being made up of a single layer (one LLISA deposition) of nanosheets or nanoflakess with similar coverage (~80%), the ultrasonicated nanoflake film absorbs 30-45% of the incident photons with energy above the excitonic peak (ca. 1.88 eV) while the ECPI-produced nanosheet film absorbs < 20%. This is consistent with the observations made using STEM (Figure 3) wherein the thicker ultrasonicated nanoflakes interact more strongly with the electron beam and thus are expected to absorb more light. Additionally, blue shifts are observed in exciton peaks A and C of the ECPI film, found at 663 nm and 433 nm, respectively, compared to 668 nm and 477 nm in the ultrasonicated film, consistent with blue shifts observed in the nanoflake dispersions (Figure S9, SI). These blue shifts suggest larger optoelectronic bandgaps as a result of fewer atomic layers in the produced nanomaterial[57,58]. Tauc plot analysis[59] confirms this hypothesis with estimated direct-transition band gap energies of ~2.4 eV for ECPI-made nanosheets and ~2.0 eV for ultrasonicated nanoflakes (Figure S12, SI). Indeed, the optical properties of these films are in direct agreement with the trends observed in STEM (Figure 3).
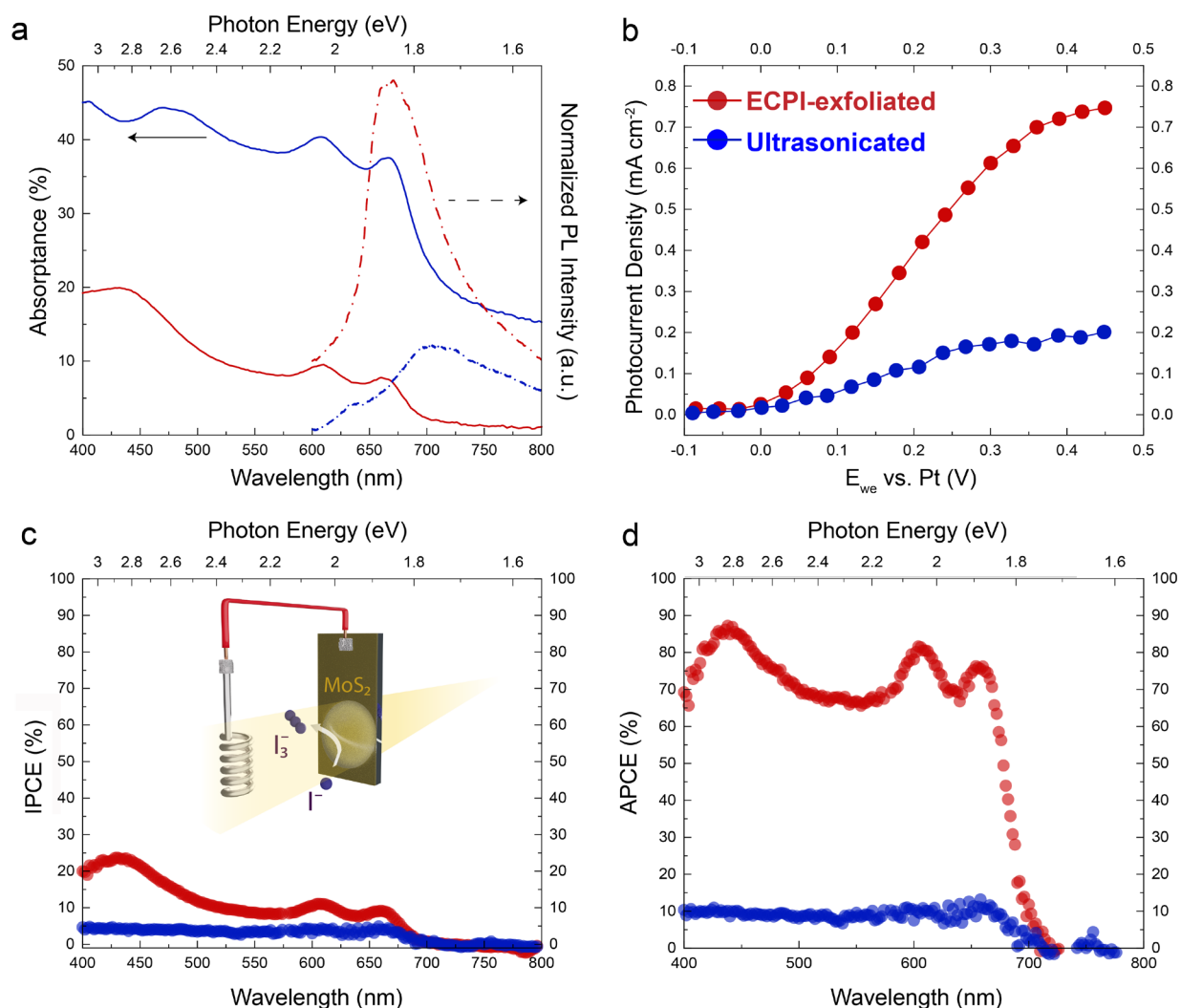
Figure 4. Optoelectronic and photoelectrochemical (PEC) properties for films of ECPI-made nanosheets (red) and sonicated nanoflakes (blue). (a) UV-Visible (solid lines) and normalized PL (dotted lines) spectra. (b) Extracted photocurrent densities for the I^-/I_3^- reaction under 1-sun light chopping conditions. (c) Incident photon-to-current conversion efficiencies (IPCEs) for the I^-/I_3^- reaction at 0.3 V vs Pt reference electrode from 400-800 nm. Inset: schematic of PEC set-up and I^-/I_3^- reaction. (d) Absorbed photon-to-current conversion efficiencies (APCEs) correct IPCE for the percentage of photons absorbed by each film.

Using laser excitation at a wavelength of 532 nm, PL can be detected for both types of MoS_2 nanosheets and is shown in Figure 4a (broken lines). The ECPI-produced nanosheets display strong PL; five-fold more than the ultrasonicated nanoflakes, when normalizing the response. In accordance with the UV-Visible, the PL displayed by the ECPI film is also blue shifted compared to the ultrasonicated film. It should be highlighted that the strong PL observed for the ECPI-made nanosheet films is achieved without any complex post-film treatments which are typically employed (*i.e. via* laser annealing,[23,60] chemical treatment,[33,61,62] *etc.*). In addition to the established lower defect density (which should reduce non-radiative recombination[63]) the higher PL can be attributed to morphology of the ECPI-made MoS_2 as thin, large-area TMD nanosheets have longer exciton lifetimes.[27] Additionally we note that PL is observed for all ECPI-produced nanosheets regardless of size and can even be modulated as a function of nanosheet thickness (Figure S13). In fact, further processing of ECPI exfoliated dispersions at high centrifuge speeds to isolate nanosheets with smaller lateral size range (< 500 nm, more similar to that of the ultrasonicated flakes) resulted in nanoflake thin films showing a sharp PL peak response (Figure S14). In contrast, the ultrasonicated nanoflakes suffer from both small lateral dimensions (which limits exciton lifetime), and higher defect densities (which increases the probability of non-radiative recombination). Together these aspects lead to fast recombination rates and renders PL difficult to detect for ultrasonicated nanoflakes.[61,64]

To compare the electron charge carrier mobility, μ_e, of thin films prepared using the ECPI exfoliation method to the standard ultrasonication, we fabricated bottom gate/bottom contact field effect transistors (FETs) by LLISA deposition of ECPI-made MoS_2 onto gold patterned SiO_2 substrates. These simple devices (see Figure S15, SI) show promising electron mobilities (saturation region) up to $\mu_{e,sat} = 0.2$ cm^2 V^{-1} s^{-1} (and an average $\mu_{e,sat} = 0.11$ cm^2 V^{-1} s^{-1} over eight

devices). Notably, this was achieved without any complex treatments, additives, or device configurations and represents a 10-fold improvement over previous work using top-contact FETs made from ultrasonication exfoliated MoS_2[36] even outperforming reports made from CVD grown MoS_2 films.[65–67] In contrast, devices prepared by the same method but with the ultrasonicated MoS_2 nanoflakes do not exhibit a gating effect (Figure S16). This can be attributed to both the small lateral nanoflake size that reduces connectivity across the transistor channel as well as defect-driven charge recombination.

The impressive UV-Visible, PL, and FET behavior of the ECPI-made nanosheets suggest that this material should exhibit superior performance in solar energy conversion applications. To demonstrate this, we fabricated simple photoelectrochemical (PEC) devices by depositing a single layer of the exfoliated MoS_2 nanosheets onto fluorine-doped tin oxide (FTO) coated glass substrates and evaluated the photo-driven oxidation of iodide (I^-) to triiodide (I_3^-) under simulated solar irradiation. The iodide/triiodide reaction (Figure 4c inset) was chosen for its simple nature and well-studied mechanism[68] compared to other potential redox couples. Moreover, iodine (I_2) can be isolated as a potentially useful product.[69] For comparison, ultrasonicated MoS_2 nanoflake film devices were fabricated and tested under the same conditions. The extracted photocurrent densities for the ECPI-made MoS_2 (red) and ultrasonicated MoS_2 (blue) are shown in Figure 4b as a function of the applied potential (the raw voltammetry data showing light and dark response can be found in Figure S17a). Films made from ECPI-exfoliated MoS_2 achieve impressive photocurrents (average of 0.9 mA cm^{-2} at +0.45 V *vs.* Pt in 50 mM LiI in acetonitrile over 12 photoanodes tested), with champion devices surpassing 1.25 mA cm^{-2} (Figure S17b). Compared to ultrasonicated nanoflake films, ECPI-prepared nanosheet films absorb less light (Figure 4a) yet have higher photocurrents (Figure 4b). Indeed at +0.3 V vs Pt, the ECPI-produced nanosheets

shown in Figure 4b achieve three times more photocurrent (0.6 mA cm^{-2}) than the sonicated nanoflakes (0.2 mA cm^{-2}). Regarding the observed dark current (Figure S17, SI) we note that some dark current is expected from the iodide oxidation reaction as a result of the catalytically active defect sites typically found on the edges of all MoS$_2$ nanomaterials. This is well established[70] and unavoidable. Notably there is less dark current in the ECPI-made nanosheets compared to the ultrasonicated nanoflakes, consistent with the conclusion that the ECPI-made sheets possess fewer defects.

Considering the lower light absorption of the ECPI-made nanosheets compared to the ultrasonicated ones suggests a large difference in the internal quantum yield between the two preparation methods. To confirm this, we estimated the photon-to-current quantum yields using monochromatic illumination between 400 and 800 nm at a photoanode bias of +0.3 V vs Pt (chosen in order to fairly compare the sonicated and ECPI-made nanoflakes since the high dark current of the ultrasonicated flakes at high voltages made extracting photocurrents unreliable). The extracted incident photon-to-current conversion efficiency (IPCE) for both exfoliation methods is shown in Figure 4c. In both cases the IPCE trace follows the absorptance spectrum of MoS$_2$, with exciton peaks A and B around 660 nm and 606 nm, respectively. However, the maximum IPCE of the ultrasonicated nanoflake photoanode (blue) is around 5% while ECPI-made nanosheet photoanode (red) shows sharp features reaching 10% near the exciton peaks A and B and nearly 25% near excitonic peak C (430 nm). The differences in the IPCE spectra are magnified when the photoanode light absorption is considered. Doing so gives the absorbed photon-to-current conversion efficiency (APCE) shown in Figure 4d. Here the superiority of the ECPI-made nanosheet film is clearly evident as it reaches 80% at 606 nm and 90% at 420 nm. Compared to sonicated films, having a maximum APCE of 10%, this is 9-fold increase. Qualitatively this agrees

well with the previous observations that the ECPI-based nanosheet thin films absorb one third of the light on average (Figure 4a) yet produce three times the photocurrent (Figure 4b). We note that applying a more positive voltage to the ECPI-made nanosheet photoanodes would lead to slightly higher IPCE and APCE values since the saturation photocurrent density of the photoanode tested was 20% higher than at the conditions tested (+0.3 V).

Compared to CVD-grown TMD monolayers tested in similar or more elaborate systems,[71–75] the powder-processed ECPI-exfoliated perform equally or better (Table S1). For example, Wang *et al.* reported a CVD grown MoS_2 monolayer with external and internal quantum efficiencies of 3.69% and 44.2%, respectively, for the iodide/triiodide redox couple at +0.5 vs Ag/AgI in 1 M NaI (~0.57 vs Pt).[72] Thus, the ECPI-made nanosheets reported herein represent benchmark solar energy conversion performance for solution processed 2D MoS_2.

Application to other layered TMD materials

As a final note, expanding the scope of the ECPI exfoliation method was demonstrated by employing it to prepare nanosheets of other TMDs such as *n*-type WS_2 and *p*-type WSe_2. In these cases, only small adjustments (including, for example, the mass of powder for the pellet and the annealing conditions) were needed to afford the successful exfoliation. Large-area and thin nanosheets were observed for the W-based TMDs without any additional treatments (Figure S18, SI). Comparing the UV-Visible and PL spectra of these ECPI exfoliated WS_2 and WSe_2 to their ultrasonicated counterparts shows similar improvements as was observed for MoS_2 (Figure S19, SI). These results underline the effectiveness of the scalable exfoliation technique reported herein and, since many 2D TMD-based devices employ van der Waals heterojunctions of more than one

TMD, this showcases the feasibility of fully solution-processed high-performance heterojunction 2D TMD devices.

CONCLUSIONS

In summary, we have presented a versatile and scalable approach for the gentle exfoliation of layered TMDs into 2D nanosheets. By processing commercially-available TMD powders into annealed pellets, we leverage the intrinsic conductivity of the material to electrochemically intercalate them with large molecule cations. In doing so we overcome size-thickness limitations experienced by other solution processable exfoliation techniques to produce very thin flakes with large lateral dimensions. While the traditionally-produced ultrasonicated nanoflakes are thick, small, and plagued by edge-steps, our ECPI-produced nanoflakes show more desirable morphology being thin, large, and with pristine, flat basal planes. These factors lead to improved optoelectronic properties including enhanced PL, exceptional charge carrier mobility, and high photocurrent density while absorbing less than 20% of the incident light. These last properties manifest as high internal quantum yields reaching 90% for the ECPI-made nanosheet photoanodes compared to just 12% for the ultrasonicated nanoflake photoanodes. Surprisingly our ECPI-made nanoflakes films even outperform CVD made flakes under similar testing conditions. Finally, we demonstrate the adaptability of this method by exfoliating W-based TMDS WS_2 and WSe_2. Like MoS_2, these materials experience improved morphology and optoelectronic properties compared to their sonication counterparts. This greatly expands the range of configurations for high-performing 2D TMD devices. Thus, this work provides an advance for the scalable production of 2D materials ideally engineered for solar-energy conversion applications.

METHODS

Pellet Pressing + Annealing. 500 mg of as-received MoS_2 powder (Sigma-Aldrich; powder < 2 μm, 99%) was pressed using a manual Beckman hydraulic pellet press, 12.5 mm diameter die, up to 10 tons and held for 5 s. It is noted that this is a standard KCl pellet press (as used for FTIR spectroscopy sample preparation) which operates by filling the die (polished plate, powder, polished plate), compressing the sandwiched powder in the die with a pushing rod, and applying the pressure *via* the press to the pressing rod to compact the pellet. The polished plates and pressed pellet are then gently removed from the die using the pushing rod.

Up to three 500 mg pellets are vacuum sealed in a fused quartz glass tube (see Figure S20, SI) with 100 mg S powder (3:1 molar ratio MoS_2:S) ensuring the pellets are not touching to avoid fusing. The pellets are heated from room temperature to 1100 °C over 8 hours, held at 1100 °C for 48 hours, then allowed to cool naturally. Similar conditions were used for WS_2. For WSe_2 better annealing results were obtained using 750 mg pellets and heating from room temperature to 1000 °C over 8 hours, holding for 12 hours, and cooling naturally. See Supporting Information, Method note 1 for additional information concerning starting mass, die diameter, and annealing conditions.

Electrochemical Pellet Intercalation and Exfoliation. The annealed pellet was clipped with an alligator clip and placed in a 50 mL beaker with a glassy carbon counter electrode. Both electrodes were connected to a potentiostat with the MoS_2 pellet as the working electrode, WE. A solution of 5 mg mL^{-1} tetraheptylammonium bromide (Acros Organics, 99%) in acetonitrile (Merck Millipore) was added until the pellet is submerged without liquid touching the alligator clip, and with sufficient space between electrodes to avoid contact as the WE expands. A voltage of 10 V was applied for 24 h (WE as cathode), during which the solution begins to turn yellow at the anode,

and the pellet begins to slowly expand and slough off. After the pellet has become a fluffy powder at the bottom of the beaker, the powder and remaining pellet was carefully collected and washed thoroughly with ethanol *via* vacuum filtration with a nylon filter (pore size 0.45 μm). The solid material is transferred to a 50 mL centrifuge tube with 10 mL of NMP (Acros Organics; 99+% for spectroscopy) before and bath sonication (Ultrasonic bath USC T, VWR, 45 kHz) in water at 25°C for 1-2 hours. Finally, the solution was centrifuged for 30 min at 120 rcf using an Eppendorf centrifuge 5810 equipped with a FA-45-6-30 rotor. The top 8 mL of supernatant is collected and transferred to a new container. See Supporting Information Method notes 2 - 6 for additional information concerning salt choice, applied voltage, intercalation time, exfoliation time, and centrifuge speed.

Ultrasonication Exfoliation. For MoS_2, 500 mg of as-received powder (Sigma-Aldrich; powder <2 μm, 99%) was sonicated in 50 mL of NMP (Acros Organics; 99+% for spectroscopy) by using a Qsonica Model Q700 probe sonicator for 2h at 50% amplitude (10 s on, 2 s off) while keeping the solution at 0.4 °C with a recirculating chiller. The resulting dispersion was first centrifuged for 30 min at 120 using an Eppendorf centrifuge 5810 equipped with a FA-45-6-30 rotor. The supernatant was collected and centrifuged at 7750 rcf for 30 min. The pellet was collected and redispersed in 10 mL (10:1 by volume) of tert-butanol:n-butanol (Sigma-Aldrich; ACS reagent >99.7%) *via* bath sonication for 30 min in ice water.

Thin Film Formation. Thin films were made *via* a liquid/liquid interface created between deionized water and hexane (Sigma-Aldrich; >99%) using a previously-described approach.[27] Transfer to substrate was accomplished by aspirating the organic phase and then either aspirating the water phase to descend the film onto a pre-positioned substrate (for FTO glass) or *via* a stamping method (for FET substrates) wherein the substrate is manipulated with a suction pen and

pressed into the film, transferring the material onto the substrate. FET substrates were cleaned by UV/O$_3$ for 10 min prior to deposition. Films were then annealed at 200 °C for 120 min in a vacuum oven to remove excess solvent.

UV-Visible / Raman / PL Spectroscopy / XPS / XRD. UV-Vis spectra were acquired using a Shimadzu UV 3600 spectrometer from 800-300 nm using an integrating sphere with step size 1 nm and slit width of 5 nm. Measurements of solutions were taken using a quartz cuvette and films were analyzed directly in transmission mode. Dispersions of nanosheets in NMP were diluted in water. The same quantity of NMP was placed in water and used for a blank. Films were measured first in transmission mode then in reflectance mode using an air blank. Inverse mode was used to collect total reflectance and double beam mode was used to avoid fluctuations within the machine. All films were measured substrate-side towards the light source to mimic PEC testing conditions. The absorption of FTO was measured and calculated separately. Absorptance was calculated as shown in equation 1 and 2:

$$\text{Absorptance } (A\%) = 100 - \%T - \%R \qquad (1)$$

$$\text{Absorptance}(MoS_2) = \text{Absorptance}(MoS_2 + FTO) - \text{Absorptance}(FTO) \qquad (2)$$

Where %T and %R are the percent transmission and reflection, respectively. Raman spectra and PL spectra were obtained using a Horiba Xplora Plus Raman microscope with 532 nm radiation (40 mW). Raman spectra were acquired from 100-1800 cm^{-1} using a 100x objective, slit of 200 μm, hole of 500 μm, a grating with 2400 gr/mm, 10% filter, 10 s of acquisition, and 5 accumulations. Note that the diameter of our excitation beam is large compared to average nanosheet size and the nanosheets are relatively densely packed on the substrate. This means the signal observed will be an average over many nanosheet sizes. PL spectra were obtained from 550-

950 nm using a 100x objective, a grating with 600gr/mm, slit of 200 µm, hole of 500 µm, 255 filter, 4s of acquisition, and 4 accumulations. Pl spectra were normalized according to Raman signals appearing around 580 nm. XPS spectra were acquired using a PHI Versa Probe II (Physical Instruments AG, Germany). Analysis was performed using a monochromatic Al Kα X-ray source operated at 50 W. The spherical mirror analyzer was set at 45° take-off angle with respect to the sample surface. The pass energy was 46.95 eV yielding a full width at half maximum of 0.91 eV for the Ag 3d 5/2 peak. Curve fitting was performed using CasaXPS software. X-ray diffraction measurements were taken in Debye-Scherrer geometry (scanning mode) using Cu-K-alpha radiation on a Bruker D8 Discover Plus instrument equipped with a rotating anode and a Dectris Eiger2 500K detector. Samples were loaded into 0.5 mm borosilicate capillaries and spun during data acquisition.

SEM / TEM / HAADF STEM / HR STEM. SEM images were acquired using a Zeiss Merlin operated at 2 kV with probe current of 100 pA, a working distance of about 2.8 mm, and using an in-lens detector. HAADF STEM images and SAED were acquired on a FEI Talos F200S microscope operated at 200 kV. HAADF STEM images were obtained using a probe current of 100 pA, a camera length of 77 mm (collection angle > 75 mrad) and a dwell of 1-2 µs. High-resolution STEM images were acquired on a FEI Titan Themis microscope operated at 80 kV and equipped with a field emission gun (X-FEG). The aberrations of the probe were corrected with a CEOS DCOR system up to the 3rd order. ADF and iDPC imaging were acquired simultaneously using a probe current of 30 pA, a camera length of 230 mm (collection angle for ADF > 35 mrad) and a dwell time of 8 µs.

2D-PAINT. Defect mapping of MoS_2 was performed by the 2D-PAINT method that has been described in detail previously.[50] Imaging was performed on a custom-built total internal reflection

fluorescence microscope with a dual-channel view optical system (DV2, Photometrics) and an EMCCD camera (iXon DU-897, Andor) that allows simultaneous recording of the specimen in the split wavelength windows of 509-530 nm and 675-725 nm. During imaging, liquid-exfoliated MoS_2 nanosheets on a coverslip are mounted in a reservoir on top of the high-NA oil-immersion objective lens (UApo Nx100, NA 1.49, Olympus). The probe, consisting of a 70 base pairs DNA oligomer with a thiol tail and an Atto 488 labeling dye is used in all experiments. The probe concentration was 1.0 nM. Illumination from a 488 nm laser (Sapphire, Coherent) was used to excite the sample and the probes. Exposure time is set as 50 ms with 500 ms sampling rate. For each experiment, 1000 frames are recorded. Post-processing of the images to localize the centroids of the defect-bound fluorophores is done by FIJI plugin ThunderStrom using integrated Gaussian PSF without multi-emitter fitting.[76] Reconstructed images were plotted using averaged shifted histograms rendering. Spatial autocorrelation analysis of the reconstructed images is performed with a MATLAB code[56] to extract Global Moran's I value with the weight matrix set as 9-by-9 pixels (equivalent to 20-by-20 nm, close to the localization uncertainty).

FET Testing. FET measurements were carried out in a nitrogen atmosphere using a custom-built probe station and a Keithley 2612A dual-channel source measure unit. Au coated SiO_2 transistor substrates (Fraunhofer ISE) were used with 10 mm channel widths (W) and an insulator capacitance (C_i) of $1.8 \cdot 10^{-8}$ F. Channel lengths (L) of 5 or 10 μm were used. Two LLISA nanosheet depositions on the substrate were used to ensure continuous nanosheet coverage. Drain voltage was scanned from 0-40 V with gate voltages from 0-40 V. The slope (m) was extracted from the device transfer curve and the charge carrier mobility, μ_{sat}, was calculated according to equation (3):

$$\mu_{sat} = \frac{2Lm^2}{WC_i} \qquad\qquad (3)$$

Photoelectrochemical Testing. Single-layer (one LLISA deposition) nanosheet films deposited

on FTO-coated glass were used as photoelectrodes directly. Linear scanning voltammetry (LSV)

measurements were obtained using a three-electrode (BioLogic SP-200 potentiostat) system with

the TMD thin film as the working electrode a glassy carbon counter electrode and a Pt

pseudoreference electrode. The active area of the electrode was 0.26 cm^2. The electrolyte was 50

mM LiI and 25 mM TBAFP (Sigma-Aldrich, 99%) in acetonitrile (Merck Millipore). Voltage was

applied from –0.3 V to +0.5 V (vs Pt) at a scan rate of 10 mV s^{-1}. A 1000W Xe light source with

water and KG2 filter (Schott) was used and calibrated to 1-sun intensity. Illumination was

intermittent during LSV measurement; on for 2s, off for 2s. All samples were measured substrate-

side towards the light source. To estimate the IPCE, photoelectrodes were measured under

illumination from a Tunable PowerArc monochromator. Incident photon power was recorded *via*

a silicon photodiode. The illumination was scanned from 650 nm to 400 nm with 2 nm steps and

2s light on and 2s light off between wavelengths while the photocurrent was recorded at +0.3 V vs

Pt.

ASSOCIATED CONTENT

Supporting Information. Supporting information available for:

- Figures S1-17
- Video S1

The Supporting Information file contains methods notes for additional details on the ECPI method
and possible adaptations. Figures S1-4 contain information related to pellet annealing and pellet
intercalation. Figures S5-9 give additional characterization of the ECPI-made and ultrasonicated
nanoflake dispersions. Figure S10 gives additional HR-TEM images for ECPI made and

ultrasonicated nanoflakes for comparison. Figure S11 gives the raw images from the optical defect mapping using the 2D PAINT method. Figures S12-14 display further characterization of the optoelectronic properties of the ECPI-made nanoflakes. Figures S16-17 display the field-effect transistor devices for ECPI-made and ultrasonicated nanoflakes as discussed in the main text. Figure S17 contains the raw LSV curves for the ultrasonicated and ECPI-made nanoflake films shown in Figure 4 of the main text. Figures S18-19 show ECPI-made nanosheets of WS_2 and WSe_2 as well as characterization of their optoelectronic properties. Figure S20 provides additional tips for performing the ECPI procedure, namely tube sealing and exfoliation. Finally, Table S1 is a reference comparing several works based on yield, nanoflake size, quantum yield, and exfoliation method.

Video S1 shows the intercalation and subsequent partial exfoliation of a MoS_2 pellet in THAB-acetonitrile.

AUTHOR INFORMATION

Corresponding Author: Kevin Sivula - Laboratory for Molecular Engineering of Optoelectronic

Nanomaterials (LIMNO), Institute of Chemical Sciences and Engineering, École Polytechnique

Fédérale de Lausanne, 1015 Lausanne, Switzerland

Orcid: http://orcid.org/0000-0002-8458-0270

Email: kevin.sivula@epfl.ch

ACKNOWLEDGMENT

REFERENCES

(1)   Alzakia, F. I.; Tan, S. C. Liquid-Exfoliated 2D Materials for Optoelectronic Applications. *Adv. Sci.* **2021**, *8* (11), 2003864. https://doi.org/10.1002/advs.202003864.

(2)   Li, J.; Yang, X.; Liu, Y.; Huang, B.; Wu, R.; Zhang, Z.; Zhao, B.; Ma, H.; Dang, W.; Wei, Z.; Wang, K.; Lin, Z.; Yan, X.; Sun, M.; Li, B.; Pan, X.; Luo, J.; Zhang, G.; Liu, Y.; Huang, Y.; Duan, X.; Duan, X. General Synthesis of Two-Dimensional van Der Waals Heterostructure Arrays. *Nature* **2020**, *579* (7799), 368–374. https://doi.org/10.1038/s41586-020-2098-y.

(3)   Liang, S.; Cheng, B.; Cui, X.; Miao, F. Van Der Waals Heterostructures for High-Performance Device Applications: Challenges and Opportunities. *Adv. Mater.* **2019**, 1903800. https://doi.org/10.1002/adma.201903800.

(4)   Lin, Z.; Huang, Y.; Duan, X. Van Der Waals Thin-Film Electronics. *Nat. Electron.* **2019**, *2* (9), 378–388. https://doi.org/10.1038/s41928-019-0301-7.

(5)   Ricciardulli, A. G.; Blom, P. W. M. Solution-Processable 2D Materials Applied in Light-Emitting Diodes and Solar Cells. *Adv. Mater. Technol.* **2020**, *5* (8), 1900972. https://doi.org/10.1002/admt.201900972.

(6)   Ganguly, P.; Harb, M.; Cao, Z.; Cavallo, L.; Breen, A.; Dervin, S.; Dionysiou, D. D.; Pillai, S. C. 2D Nanomaterials for Photocatalytic Hydrogen Production. *ACS Energy Lett.* **2019**, *4* (7), 1687–1709. https://doi.org/10.1021/acsenergylett.9b00940.

(7)   Li, C.; Cao, Q.; Wang, F.; Xiao, Y.; Li, Y.; Delaunay, J.-J.; Zhu, H. Engineering Graphene and TMDs Based van Der Waals Heterostructures for Photovoltaic and Photoelectrochemical Solar Energy Conversion. *Chem. Soc. Rev.* **2018**, *47* (13), 4981–5037. https://doi.org/10.1039/C8CS00067K.

(8)   Yu, X.; Prévot, M. S.; Guijarro, N.; Sivula, K. Self-Assembled 2D WSe_2 Thin Films for Photoelectrochemical Hydrogen Production. *Nat. Commun.* **2015**, *6*, 7596. https://doi.org/10.1038/ncomms8596.

(9)   Wells, R. A.; Johnson, H.; Lhermitte, C. R.; Kinge, S.; Sivula, K. Roll-to-Roll Deposition of Semiconducting 2D Nanoflake Films of Transition Metal Dichalcogenides for Optoelectronic Applications. *ACS Appl. Nano Mater.* **2019**, *2* (12), 7705–7712. https://doi.org/10.1021/acsanm.9b01774.

(10) Xu, X.; Pan, Y.; Liu, S.; Han, B.; Gu, P.; Li, S.; Xu, W.; Peng, Y.; Han, Z.; Chen, J.; Gao, P.; Ye, Y. Seeded 2D Epitaxy of Large-Area Single-Crystal Films of the van Der Waals Semiconductor 2H MoTe2. *Science* **2021**, *372* (6538), 195–200. https://doi.org/10.1126/science.abf5825.

(11) Lin, Z.; Liu, Y.; Halim, U.; Ding, M.; Liu, Y.; Wang, Y.; Jia, C.; Chen, P.; Duan, X.; Wang, C.; Song, F.; Li, M.; Wan, C.; Huang, Y.; Duan, X. Solution-Processable 2D Semiconductors for High-Performance Large-Area Electronics. *Nature* **2018**, *562* (7726), 254–258. https://doi.org/10.1038/s41586-018-0574-4.

(12) Yu, X.; Sivula, K. Toward Large-Area Solar Energy Conversion with Semiconducting 2D Transition Metal Dichalcogenides. *ACS Energy Lett.* **2016**, *1* (1), 315–322. https://doi.org/10.1021/acsenergylett.6b00114.

(13) Nicolosi, V.; Chhowalla, M.; Kanatzidis, M. G.; Strano, M. S.; Coleman, J. N. Liquid Exfoliation of Layered Materials. *Science* **2013**, *340* (6139), 1226419. https://doi.org/10.1126/science.1226419.

(14) Lee, Y.-H.; Zhang, X.-Q.; Zhang, W.; Chang, M.-T.; Lin, C.-T.; Chang, K.-D.; Yu, Y.-C.; Wang, J. T.-W.; Chang, C.-S.; Li, L.-J.; Lin, T.-W. Synthesis of Large-Area MoS_2 Atomic Layers with Chemical Vapor Deposition. *Adv. Mater.* **2012**, *24* (17), 2320–2325. https://doi.org/10.1002/adma.201104798.

(15) Zhan, Y.; Liu, Z.; Najmaei, S.; Ajayan, P. M.; Lou, J. Large-Area Vapor-Phase Growth and Characterization of MoS2 Atomic Layers on a SiO2 Substrate. *Small* **2012**, *8* (7), 966–971. https://doi.org/10.1002/smll.201102654.

(16) Fu, D.; Zhao, X.; Zhang, Y.-Y.; Li, L.; Xu, H.; Jang, A.-R.; Yoon, S. I.; Song, P.; Poh, S. M.; Ren, T.; Ding, Z.; Fu, W.; Shin, T. J.; Shin, H. S.; Pantelides, S. T.; Zhou, W.; Loh, K. P. Molecular Beam Epitaxy of Highly Crystalline Monolayer Molybdenum Disulfide on Hexagonal Boron Nitride. *J. Am. Chem. Soc.* **2017**, *139* (27), 9392–9400. https://doi.org/10.1021/jacs.7b05131.

(17) Wang, Q. H.; Kalantar-Zadeh, K.; Kis, A.; Coleman, J. N.; Strano, M. S. Electronics and Optoelectronics of Two-Dimensional Transition Metal Dichalcogenides. *Nat. Nanotechnol.* **2012**, *7* (11), 699–712. https://doi.org/10.1038/nnano.2012.193.

(18) Bonneau, P. R.; Wiley, J. B.; Kaner, R. B.; Mansuktto, M. F. Metathetical Precursor Route to Molybdenum Disulfide. In *Inorganic Syntheses*; John Wiley & Sons, Ltd: New York, 1995; pp 33–37. https://doi.org/10.1002/9780470132616.ch8.

(19) Coleman, J. N.; Lotya, M.; O'Neill, A.; Bergin, S. D.; King, P. J.; Khan, U.; Young, K.; Gaucher, A.; De, S.; Smith, R. J.; Shvets, I. V.; Arora, S. K.; Stanton, G.; Kim, H.-Y.; Lee, K.; Kim, G. T.; Duesberg, G. S.; Hallam, T.; Boland, J. J.; Wang, J. J.; Donegan, J. F.; Grunlan, J. C.; Moriarty, G.; Shmeliov, A.; Nicholls, R. J.; Perkins, J. M.; Grieveson, E. M.; Theuwissen, K.; McComb, D. W.; Nellist, P. D.; Nicolosi, V. Two-Dimensional Nanosheets Produced by Liquid Exfoliation of Layered Materials. *Science* **2011**, *331* (6017), 568–571. https://doi.org/10.1126/science.1194975.

(20) Backes, C.; Higgins, T. M.; Kelly, A.; Boland, C.; Harvey, A.; Hanlon, D.; Coleman, J. N. Guidelines for Exfoliation, Characterization and Processing of Layered Materials Produced by Liquid Exfoliation. *Chem. Mater.* **2017**, *29* (1), 243–255. https://doi.org/10.1021/acs.chemmater.6b03335.

(21) Forsberg, V.; Zhang, R.; Bäckström, J.; Dahlström, C.; Andres, B.; Norgren, M.; Andersson, M.; Hummelgård, M.; Olin, H. Exfoliated MoS_2 in Water without Additives. *PLoS ONE* **2016**, *11* (4). https://doi.org/10.1371/journal.pone.0154522.

(22) Varrla, E.; Backes, C.; Paton, K. R.; Harvey, A.; Gholamvand, Z.; McCauley, J.; Coleman, J. N. Large-Scale Production of Size-Controlled MoS_2 Nanosheets by Shear Exfoliation. *Chem. Mater.* **2015**, *27* (3), 1129–1139. https://doi.org/10.1021/cm5044864.

(23) Eda, G.; Yamaguchi, H.; Voiry, D.; Fujita, T.; Chen, M.; Chhowalla, M. Photoluminescence from Chemically Exfoliated MoS2. *Nano Lett.* **2011**, *11* (12), 5111–5116. https://doi.org/10.1021/nl201874w.

(24) Fan, X.; Xu, P.; Li, Y. C.; Zhou, D.; Sun, Y.; Nguyen, M. A. T.; Terrones, M.; Mallouk, T. E. Controlled Exfoliation of MoS_2 Crystals into Trilayer Nanosheets. *J. Am. Chem. Soc.* **2016**, *138* (15), 5143–5149. https://doi.org/10.1021/jacs.6b01502.

(25) Das, S. K.; Gawas, R.; Chakrabarty, S.; Harini, G.; Patidar, R.; Jasuja, K. An Unexpected Transformation of Organic Solvents into 2D Fluorescent Quantum Dots during

Ultrasonication-Assisted Liquid-Phase Exfoliation. *J. Phys. Chem. C* **2019**, *123* (41), 25412–25421. https://doi.org/10.1021/acs.jpcc.9b03975.

(26) O'Neill, A.; Khan, U.; Coleman, J. N. Preparation of High Concentration Dispersions of Exfoliated MoS$_2$ with Increased Flake Size. *Chem. Mater.* **2012**, *24* (12), 2414–2421. https://doi.org/10.1021/cm301515z.

(27) Yu, X.; Sivula, K. Photogenerated Charge Harvesting and Recombination in Photocathodes of Solvent-Exfoliated WSe$_2$. *Chem. Mater.* **2017**, *29* (16), 6863–6875. https://doi.org/10.1021/acs.chemmater.7b02018.

(28) Zheng, W.; Lee, L. Y. S. Beyond Sonication: Advanced Exfoliation Methods for Scalable Production of 2D Materials. *Matter* **2022**, *0* (0). https://doi.org/10.1016/j.matt.2021.12.010.

(29) Cheng, Y.; Nie, A.; Zhang, Q.; Gan, L.-Y.; Shahbazian-Yassar, R.; Schwingenschlogl, U. Origin of the Phase Transition in Lithiated Molybdenum Disulfide. *ACS Nano* **2014**, *8* (11), 11447–11453. https://doi.org/10.1021/nn505668c.

(30) Er, E.; Hou, H.-L.; Criado, A.; Langer, J.; Möller, M.; Erk, N.; Liz-Marzán, L. M.; Prato, M. High-Yield Preparation of Exfoliated 1T-MoS$_2$ with SERS Activity. *Chem. Mater.* **2019**, *31* (15), 5725–5734. https://doi.org/10.1021/acs.chemmater.9b01698.

(31) Ejigu, A.; Kinloch, I. A.; Prestat, E.; Dryfe, R. A. W. A Simple Electrochemical Route to Metallic Phase Trilayer MoS$_2$: Evaluation as Electrocatalysts and Supercapacitors. *J. Mater. Chem. A* **2017**, *5* (22), 11316–11330. https://doi.org/10.1039/C7TA02577G.

(32) Yu, X.; Guijarro, N.; Johnson, M.; Sivula, K. Defect Mitigation of Solution-Processed 2D WSe$_2$ Nanoflakes for Solar-to-Hydrogen Conversion. *Nano Lett.* **2018**, *18* (1), 215–222. https://doi.org/10.1021/acs.nanolett.7b03948.

(33) Zhao, Y.; Gali, S. M.; Wang, C.; Pershin, A.; Slassi, A.; Beljonne, D.; Samorì, P. Molecular Functionalization of Chemically Active Defects in WSe$_2$ for Enhanced Opto-Electronics. *Adv. Funct. Mater.* **2020** *30* (45), 2005045. https://doi.org/10.1002/adfm.202005045.

(34) Fan, X.; Xu, P.; Zhou, D.; Sun, Y.; Li, Y. C.; Nguyen, M. A. T.; Terrones, M.; Mallouk, T. E. Fast and Efficient Preparation of Exfoliated 2H MoS$_2$ Nanosheets by Sonication-Assisted Lithium Intercalation and Infrared Laser-Induced 1T to 2H Phase Reversion. *Nano Lett.* **2015**, *15* (9), 5956–5960. https://doi.org/10.1021/acs.nanolett.5b02091.

(35) Chou, S. S.; De, M.; Kim, J.; Byun, S.; Dykstra, C.; Yu, J.; Huang, J.; Dravid, V. P. Ligand Conjugation of Chemically Exfoliated MoS$_2$. *J. Am. Chem. Soc.* **2013**, *135* (12), 4584–4587. https://doi.org/10.1021/ja310929s.

(36) Yu, X.; Prévot, M. S.; Sivula, K. Multiflake Thin Film Electronic Devices of Solution Processed 2D MoS$_2$ Enabled by Sonopolymer Assisted Exfoliation and Surface Modification. *Chem. Mater.* **2014**, *26* (20), 5892–5899. https://doi.org/10.1021/cm502378g.

(37) Hu, R.; Huang, Z.; Wang, B.; Qiao, H.; Qi, X. Electrochemical Exfoliation of Molybdenum Disulfide Nanosheets for High-Performance Supercapacitors. *J. Mater. Sci. Mater. Electron.* **2021**, *32* (6), 7237–7248. https://doi.org/10.1007/s10854-021-05432-5.

(38) Golub, A. S.; Zubavichus, Ya. V.; Slovokhotov, Yu. L.; Novikov, Yu. N.; Danot, M. Layered Compounds Assembled from Molybdenum Disulfide Single-Layers and Alkylammonium Cations. *Solid State Ion.* **2000**, *128* (1), 151–160. https://doi.org/10.1016/S0167-2738(99)00347-1.

(39) Stepanov, A. A.; Lenenko, N. D.; Golub', A. S.; Pervov, V. S. Synthesis of Layered Metal Dichalcogenides with Organic Cations by Electrochemical Reduction in Suspensions. *Russ. J. Electrochem.* **2013**, *49* (1), 86–90. https://doi.org/10.1134/S1023193513010138.

(40) Li, J.; Song, P.; Zhao, J.; Vaklinova, K.; Zhao, X.; Li, Z.; Qiu, Z.; Wang, Z.; Lin, L.; Zhao, M.; Herng, T. S.; Zuo, Y.; Jonhson, W.; Yu, W.; Hai, X.; Lyu, P.; Xu, H.; Yang, H.; Chen, C.; Pennycook, S. J.; Ding, J.; Teng, J.; Castro Neto, A. H.; Novoselov, K. S.; Lu, J. Printable Two-Dimensional Superconducting Monolayers. *Nat. Mater.* **2020**, 1–7. https://doi.org/10.1038/s41563-020-00831-1.

(41) Tsai, M.-L.; Su, S.-H.; Chang, J.-K.; Tsai, D.-S.; Chen, C.-H.; Wu, C.-I.; Li, L.-J.; Chen, L.-J.; He, J.-H. Monolayer MoS₂ Heterojunction Solar Cells. *ACS Nano* **2014**, *8* (8), 8317–8322. https://doi.org/10.1021/nn502776h.

(42) Pesci, F. M.; Sokolikova, M. S.; Grotta, C.; Sherrell, P. C.; Reale, F.; Sharda, K.; Ni, N.; Palczynski, P.; Mattevi, C. MoS₂/WS₂ Heterojunction for Photoelectrochemical Water Oxidation. *ACS Catal.* **2017**, *7* (8), 4990–4998. https://doi.org/10.1021/acscatal.7b01517.

(43) LeBeau, J. M.; Findlay, S. D.; Allen, L. J.; Stemmer, S. Quantitative STEM: Experimental Methods and Applications. *J. Phys. Conf. Ser.* **2012**, *371*, 012053. https://doi.org/10.1088/1742-6596/371/1/012053.

(44) Kang, J.; Seo, J.-W. T.; Alducin, D.; Ponce, A.; Yacaman, M. J.; Hersam, M. C. Thickness Sorting of Two-Dimensional Transition Metal Dichalcogenides via Copolymer-Assisted Density Gradient Ultracentrifugation. *Nat. Commun.* **2014**, *5* (1), 5478. https://doi.org/10.1038/ncomms6478.

(45) Powell, C. X-Ray Photoelectron Spectroscopy Database XPS,Version 4.1, NIST Standard Reference Database 20, 1989. https://doi.org/10.18434/T4T88K.

(46) Attanayake, N. H.; Thenuwara, A. C.; Patra, A.; Aulin, Y. V.; Tran, T. M.; Chakraborty, H.; Borguet, E.; Klein, M. L.; Perdew, J. P.; Strongin, D. R. Effect of Intercalated Metals on the Electrocatalytic Activity of 1T-MoS₂ for the Hydrogen Evolution Reaction. *ACS Energy Lett.* **2018**, *3* (1), 7–13. https://doi.org/10.1021/acsenergylett.7b00865.

(47) Velazquez, J. M.; John, J.; Esposito, D. V.; Pieterick, A.; Pala, R.; Sun, G.; Zhou, X.; Huang, Z.; Ardo, S.; Soriaga, M. P.; Brunschwig, B. S.; Lewis, N. S. A Scanning Probe Investigation of the Role of Surface Motifs in the Behavior of P-WSe₂ Photocathodes. *Energy Environ. Sci.* **2016**, *9* (1), 164–175. https://doi.org/10.1039/C5EE02530C.

(48) Lazić, I.; Bosch, E. G. T.; Lazar, S. Phase Contrast STEM for Thin Samples: Integrated Differential Phase Contrast. *Ultramicroscopy* **2016**, *160*, 265–280. https://doi.org/10.1016/j.ultramic.2015.10.011.

(49) Zhou, W.; Zou, X.; Najmaei, S.; Liu, Z.; Shi, Y.; Kong, J.; Lou, J.; Ajayan, P. M.; Yakobson, B. I.; Idrobo, J.-C. Intrinsic Structural Defects in Monolayer Molybdenum Disulfide. *Nano Lett.* **2013**, *13* (6), 2615–2622. https://doi.org/10.1021/nl4007479.

(50) Zhang, M.; Lihter, M.; Chen, T.-H.; Macha, M.; Rayabharam, A.; Banjac, K.; Zhao, Y.; Wang, Z.; Zhang, J.; Comtet, J.; Aluru, N. R.; Lingenfelder, M.; Kis, A.; Radenovic, A. Super-Resolved Optical Mapping of Reactive Sulfur-Vacancies in Two-Dimensional Transition Metal Dichalcogenides. *ACS Nano* **2021**, *15* (4), 7168–7178. https://doi.org/10.1021/acsnano.1c00373.

(51) Hong, J.; Hu, Z.; Probert, M.; Li, K.; Lv, D.; Yang, X.; Gu, L.; Mao, N.; Feng, Q.; Xie, L.; Zhang, J.; Wu, D.; Zhang, Z.; Jin, C.; Ji, W.; Zhang, X.; Yuan, J.; Zhang, Z. Exploring Atomic Defects in Molybdenum Disulphide Monolayers. *Nat. Commun.* **2015**, *6* (1), 6293. https://doi.org/10.1038/ncomms7293.

(52) Lin, J.; Pantelides, S. T.; Zhou, W. Vacancy-Induced Formation and Growth of Inversion Domains in Transition-Metal Dichalcogenide Monolayer. *ACS Nano* **2015**, *9* (5), 5189–5197. https://doi.org/10.1021/acsnano.5b00554.

(53) Qiu, H.; Xu, T.; Wang, Z.; Ren, W.; Nan, H.; Ni, Z.; Chen, Q.; Yuan, S.; Miao, F.; Song, F.; Long, G.; Shi, Y.; Sun, L.; Wang, J.; Wang, X. Hopping Transport through Defect-Induced Localized States in Molybdenum Disulphide. *Nat. Commun.* **2013**, *4* (1), 2642. https://doi.org/10.1038/ncomms3642.

(54) Vancsó, P.; Magda, G. Z.; Pető, J.; Noh, J.-Y.; Kim, Y.-S.; Hwang, C.; Biró, L. P.; Tapasztó, L. The Intrinsic Defect Structure of Exfoliated MoS_2 Single Layers Revealed by Scanning Tunneling Microscopy. *Sci. Rep.* **2016**, *6* (1), 29726. https://doi.org/10.1038/srep29726.

(55) Thompson, E. S.; Saveyn, P.; Declercq, M.; Meert, J.; Guida, V.; Eads, C. D.; Robles, E. S. J.; Britton, M. M. Characterisation of Heterogeneity and Spatial Autocorrelation in Phase Separating Mixtures Using Moran's I. *J. Colloid Interface Sci.* **2018**, *513*, 180–187. https://doi.org/10.1016/j.jcis.2017.10.115.

(56) Moran's I - File Exchange - MATLAB Central https://www.mathworks.com/matlabcentral/fileexchange/13663-moran-s-i (accessed 2021 -10 -19).

(57) Splendiani, A.; Sun, L.; Zhang, Y.; Li, T.; Kim, J.; Chim, C.-Y.; Galli, G.; Wang, F. Emerging Photoluminescence in Monolayer MoS_2. *Nano Lett.* **2010**, *10* (4), 1271–1275. https://doi.org/10.1021/nl903868w.

(58) Tsai, H.-S.; Huang, Y.-H.; Tsai, P.-C.; Chen, Y.-J.; Ahn, H.; Lin, S.-Y.; Lu, Y.-J. Ultrafast Exciton Dynamics in Scalable Monolayer MoS_2 Synthesized by Metal Sulfurization. *ACS Omega* **2020**, *5* (19), 10725–10730. https://doi.org/10.1021/acsomega.0c00187.

(59) Makuła, P.; Pacia, M.; Macyk, W. How To Correctly Determine the Band Gap Energy of Modified Semiconductor Photocatalysts Based on UV–Vis Spectra. *J. Phys. Chem. Lett.* **2018**, *9* (23), 6814–6817. https://doi.org/10.1021/acs.jpclett.8b02892.

(60) Ardekani, H.; Younts, R.; Yu, Y.; Cao, L.; Gundogdu, K. Reversible Photoluminescence Tuning by Defect Passivation via Laser Irradiation on Aged Monolayer MoS_2. *ACS Appl. Mater. Interfaces* **2019**, *11* (41), 38240–38246. https://doi.org/10.1021/acsami.9b10688.

(61) Amani, M.; Lien, D.-H.; Kiriya, D.; Xiao, J.; Azcatl, A.; Noh, J.; Madhvapathy, S. R.; Addou, R.; Kc, S.; Dubey, M.; Cho, K.; Wallace, R. M.; Lee, S.-C.; He, J.-H.; Ager, J. W.; Zhang, X.; Yablonovitch, E.; Javey, A. Near-Unity Photoluminescence Quantum Yield in MoS_2. *Science* **2015**, *350* (6264), 1065–1068. https://doi.org/10.1126/science.aad2114.

(62) Kim, H.; Lien, D.-H.; Amani, M.; Ager, J. W.; Javey, A. Highly Stable Near-Unity Photoluminescence Yield in Monolayer MoS_2 by Fluoropolymer Encapsulation and Superacid Treatment. *ACS Nano* **2017**, *11* (5), 5179–5185. https://doi.org/10.1021/acsnano.7b02521.

(63) Kam, K. K.; Parkinson, B. A. Detailed Photocurrent Spectroscopy of the Semiconducting Group VIB Transition Metal Dichalcogenides. *J. Phys. Chem.* **1982**, *86* (4), 463–467. https://doi.org/10.1021/j100393a010.

(64) Tsokkou, D.; Yu, X.; Sivula, K.; Banerji, N. The Role of Excitons and Free Charges in the Excited-State Dynamics of Solution-Processed Few-Layer MoS_2 Nanoflakes. *J. Phys. Chem. C* **2016**, *120* (40), 23286–23292. https://doi.org/10.1021/acs.jpcc.6b09267.

(65) Gurarslan, A.; Yu, Y.; Su, L.; Yu, Y.; Suarez, F.; Yao, S.; Zhu, Y.; Ozturk, M.; Zhang, Y.; Cao, L. Surface-Energy-Assisted Perfect Transfer of Centimeter-Scale Monolayer and Few-Layer MoS_2 Films onto Arbitrary Substrates. *ACS Nano* **2014**, *8* (11), 11522–11528. https://doi.org/10.1021/nn5057673.

(66) Lee, Y.; Yang, J.; Lee, D.; Kim, Y.-H.; Park, J.-H.; Kim, H.; Cho, J. H. Trap-Induced Photoresponse of Solution-Synthesized MoS$_2$. *Nanoscale* **2016**, *8* (17), 9193–9200. https://doi.org/10.1039/C6NR00654J.

(67) George, A. S.; Mutlu, Z.; Ionescu, R.; Wu, R. J.; Jeong, J. S.; Bay, H. H.; Chai, Y.; Mkhoyan, K. A.; Ozkan, M.; Ozkan, C. S. Wafer Scale Synthesis and High Resolution Structural Characterization of Atomically Thin MoS$_2$ Layers. *Adv. Funct. Mater.* **2014**, *24* (47), 7461–7466. https://doi.org/10.1002/adfm.201402519.

(68) Boschloo, G.; Hagfeldt, A. Characteristics of the Iodide/Triiodide Redox Mediator in Dye-Sensitized Solar Cells. *Acc. Chem. Res.* **2009**, *42* (11), 1819–1826. https://doi.org/10.1021/ar900138m.

(69) Yao, L.; Liu, Y.; Cho, H.-H.; Xia, M.; Sekar, A.; Darwich, B. P.; Wells, R. A.; Yum, J.-H.; Ren, D.; Grätzel, M.; Guijarro, N.; Sivula, K. A Hybrid Bulk-Heterojunction Photoanode for Direct Solar-to-Chemical Conversion. *Energy Environ. Sci.* **2021**, *14* (5), 3141–3151. https://doi.org/10.1039/D1EE00152C.

(70) Li, G.; Zhang, D.; Qiao, Q.; Yu, Y.; Peterson, D.; Zafar, A.; Kumar, R.; Curtarolo, S.; Hunte, F.; Shannon, S.; Zhu, Y.; Yang, W.; Cao, L. All The Catalytic Active Sites of MoS$_2$ for Hydrogen Evolution. *J. Am. Chem. Soc.* **2016**, *138* (51), 16632–16638. https://doi.org/10.1021/jacs.6b05940.

(71) Yu, W. J.; Vu, Q. A.; Oh, H.; Nam, H. G.; Zhou, H.; Cha, S.; Kim, J.-Y.; Carvalho, A.; Jeong, M.; Choi, H.; Castro Neto, A. H.; Lee, Y. H.; Duan, X. Unusually Efficient Photocurrent Extraction in Monolayer van Der Waals Heterostructure by Tunnelling through Discretized Barriers. *Nat. Commun.* **2016**, *7* (1), 13278. https://doi.org/10.1038/ncomms13278.

(72) Wang, L.; Tahir, M.; Chen, H.; Sambur, J. B. Probing Charge Carrier Transport and Recombination Pathways in Monolayer MoS$_2$/WS$_2$ Heterojunction Photoelectrodes. *Nano Lett.* **2019**, *19* (12), 9084–9094. https://doi.org/10.1021/acs.nanolett.9b04209.

(73) Yu, W. J.; Liu, Y.; Zhou, H.; Yin, A.; Li, Z.; Huang, Y.; Duan, X. Highly Efficient Gate-Tunable Photocurrent Generation in Vertical Heterostructures of Layered Materials. *Nat. Nanotechnol.* **2013**, *8* (12), 952–958. https://doi.org/10.1038/nnano.2013.219.

(74) Britnell, L.; Ribeiro, R. M.; Eckmann, A.; Jalil, R.; Belle, B. D.; Mishchenko, A.; Kim, Y.-J.; Gorbachev, R. V.; Georgiou, T.; Morozov, S. V.; Grigorenko, A. N.; Geim, A. K.; Casiraghi, C.; Neto, A. H. C.; Novoselov, K. S. Strong Light-Matter Interactions in Heterostructures of Atomically Thin Films. *Science* **2013**, *340* (6138), 1311–1314. https://doi.org/10.1126/science.1235547.

(75) Wang, L.; Schmid, M.; Nilsson, Z. N.; Tahir, M.; Chen, H.; Sambur, J. B. Laser Annealing Improves the Photoelectrochemical Activity of Ultrathin MoSe$_2$ Photoelectrodes. *ACS Appl. Mater. Interfaces* **2019**, *11* (21), 19207–19217. https://doi.org/10.1021/acsami.9b04785.

(76) Ovesný, M.; Křížek, P.; Borkovec, J.; Švindrych, Z.; Hagen, G. M. ThunderSTORM: A Comprehensive ImageJ Plug-in for PALM and STORM Data Analysis and Super-Resolution Imaging. *Bioinformatics* **2014**, *30* (16), 2389–2390. https://doi.org/10.1093/bioinformatics/btu202.